

1 **Czochralski growth and characterization of**
2 **Tb_xGd_{1-x}ScO₃ and Tb_xDy_{1-x}ScO₃ solid-solution single crystals**

3
4 C. Gugushev ^{a,*}, J. Hidde ^a, T. M. Gesing ^{b,c},
5 M. Gogolin ^b, D. Klimm ^a
6

7 ^a Leibniz Institute for Crystal Growth, Max-Born-Str. 2, 12489 Berlin, Germany.
8

9 ^b University of Bremen, Solid State Chemical Crystallography, Institute of Inorganic Chemistry
10 and Crystallography, Leobener Str. 7, 28359 Bremen, Germany
11

12 ^c University of Bremen, MAPEX Center for Materials and Processes, Bibliothekstraße 1, 28359
13 Bremen, Germany
14

15 **Abstract**
16

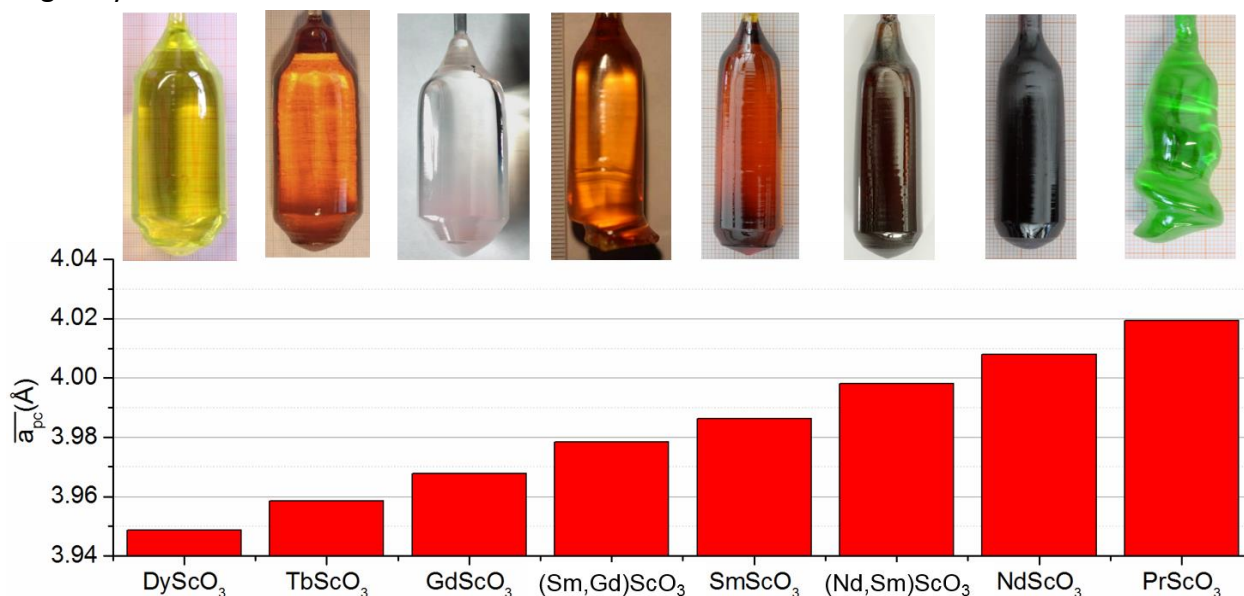
17 Tb_xGd_{1-x}ScO₃ and Tb_xDy_{1-x}ScO₃ solid-solution single crystals were grown by the Czochralski
18 method to validate the practicability of solid solutions between neighboring RE scandates
19 (REScO₃). Within this material family, it is demonstrated that a fine-tuning of the pseudo-cubic
20 lattice parameters between nearly all endmembers is now possible by adjustments of the
21 chemical composition of the mixed crystals. Therefore, film-tailored substrate lattice spacings
22 potentially allow fine adjustments of epitaxial strain or the growth of nearly strain-free
23 heteroepitaxial films. Investigations of the chemical composition of the grown crystals revealed
24 low segregation, which qualifies the solid-solutions as suitable substrate materials. The melting
25 behavior was studied by differential thermal analysis. To calculate thermal conductivity $\lambda(T)$,
26 heat capacity and thermal diffusivity were measured by differential scanning calorimetry and
27 laser flash technique, respectively. It was found that the thermal conductivity shows a minimum
28 near 900 K and increases untypically at higher temperature.
29

30 * Corresponding author. E-mail address: christo.gugushev@ikz-berlin.de (C. Gugushev)

31
32 **1. Introduction**
33

34 For more than a decade, established rare-earth (RE) scandate (REScO₃) single crystals served in
35 shape of epi-ready substrates, as basis for the development of advanced epitaxially grown films
36 with interesting ferroelectric, ferromagnetic, piezoelectric, multiferroic, or simply electronic
37 properties. The pseudo-cubic lattice parameters of the RE scandate endmembers with RE = Dy
38 to Pr range between 3.946 and 4.026 Å¹ and vary in about 0.01 Å steps as the RE series is

39 traversed (Fig. 1). Two members of RE scandates were problematic in the past: (1) PmScO_3 since
40 it is radioactive and (2) EuScO_3 , which due to the multivalent nature of Eu is thermodynamically
41 unstable in direct contact with silicon ². To facilitate an interruption free lattice parameter
42 continuity both scandates were replaced by $(\text{Nd}_{0.5}\text{Sm}_{0.5})\text{ScO}_3$ and $(\text{Sm}_{0.5}\text{Gd}_{0.5})\text{ScO}_3$ solid-solution
43 single crystals ¹.



44
45 Fig. 1 Pseudo-cubic lattice parameters of the REScO_3 endmembers and solid solution crystals
46 grown in our laboratory using the Czochralski method ^{1, 3, 4}. A part of the figure is reproduced
47 from the work of Uecker et al. ¹ with permission from the Institute of Physics, Polish Academy of
48 Science.

49
50 In the present report we investigated whether solid solutions (SSLs) utilizing REs adjacent to
51 TbScO_3 can be grown. The neighbors DyScO_3 and GdScO_3 have the largest market share of all
52 rare-earth scandates that are commercially available, and consequently options for improved
53 fine tuning of lattice parameters in the range of 3.95 to 3.97 Å (Fig. 1) are welcome. Based on
54 Vegard's rule the lattice parameters should lie properly between the values of the endmembers
55 if prepared in a 1:1 molar composition ratio.

56 57 2. Material and methods

58 59 2.1 Bulk single crystal growth

60
61 For the preparation of the starting materials, dried powders of Gd_2O_3 , Dy_2O_3 , Sc_2O_3 and Tb_4O_7
62 with purities of 99.99% (4N) were used. The powders were weighed and mixed in the following
63 nominal compositions: $\text{Tb}_x\text{Gd}_{1-x}\text{ScO}_3$ and $\text{Tb}_x\text{Dy}_{1-x}\text{ScO}_3$ with $x = 0.5$. Subsequently, to optimize
64 the crucible filling process cylindrical bars were made by cold isostatic pressing at 0.2 GPa.

65 The crystal growth experiments were performed using a conventional RF-heated Czochralski
66 set-up equipped with a crystal balance and automatic diameter control. The atmosphere during
67 growth was 5N nitrogen under ambient pressure. Iridium crucibles (inner diameter: 38 mm,
68 height: 41 mm) embedded in ZrO_2 and Al_2O_3 insulation were used. A conical baffle and an
69 actively heated iridium afterheater were placed on top of the crucibles. A growth rate of 1
70 $mm\ h^{-1}$ and a rotation rate of 10 -15 rpm were utilized. Single crystalline $DyScO_3$ and $GdScO_3$
71 seeds were used for the growth experiments.

72
73

74 2.2 Chemical and structural analyses

75

76 Segregation was investigated by micro X-ray fluorescence (μ -XRF) elemental mappings on the
77 longitudinally cut crystals. The measurements were performed at low-vacuum conditions (about
78 1 mbar) using a Bruker M4 TORNADO spectrometer. Polycapillary X-ray optics were used to
79 focus the Bremsstrahlung at the surface of the sample, which enables a high spatial resolution
80 of 25 μm . The samples were scanned by using spot distances of 53 μm for a surface area of 66.6
81 \times 41.4 mm^2 . The measurement time per point was set to 10 ms and all spots were measured six
82 times to improve the counting statistics, i.e. six passes of the scans were performed. For the
83 accurate determination of the segregation profiles, automated line scan measurements were
84 carried out along the boules central axes, i.e. between seed and end of the crystal. For these
85 measurements, the XRF spectrometer was calibrated using standard sections of known
86 composition and the duration per point measurement was set to 200 s. Each line scan consisted
87 of a series of at least 44 measurements. To determine the typical μ -XRF measurement accuracy,
88 6-fold determinations of seed-near sections were performed. For Sc, Tb, Gd and Dy, the sigma
89 values were less than or equal to 0.015, 0.011, 0.006, 0.003 at%, respectively.

90 The chemical compositions of seed-near standard sections were measured using an inductively
91 coupled plasma-optical emission spectrometer (ICP-OES) IRIS Intrepid HR Duo. The ball-milled
92 samples were dissolved by microwave digestion with a mixture of HNO_3 and H_2O_2 (220 $^\circ C$, 20
93 min). The spectrometer was calibrated with synthetic solution standards. To ensure high
94 accuracy, the sample matrix matched the calibration standard and six-fold determinations were
95 performed.

96 For the single crystal X-ray diffraction investigations bigger parts of the shoulders were crushed
97 into small fragments. One fragment of each sample was optically selected. The specimens were
98 glued to the tip of a 50 μm glass fiber and a full sphere of data was collected on a Bruker D8
99 Venture diffractometer with monochromatic $MoK\alpha_1$ ($\lambda_{K\alpha_1} = 0.710747(6)\ \text{\AA}$) radiation. Further
100 details are given in Table 1. The crystal structure solution and refinements were carried out
101 using SHELX-97 software ⁵. The lattice parameters obtained from single crystal XRD were
102 replaced by the more accurate powder XRD lattice parameters generally showing the better
103 overall statistics and less absorption effects. Beside the positional parameters, anisotropic

104 displacement ellipsoids were refined for all atoms. The corresponding refinement results are
 105 given in Table 2.

106 Table 1: Experimental data of Tb_{0.5}Gd_{0.5}ScO₃ and Tb_{0.5}Dy_{0.5}ScO₃.

Solid solution crystal	Tb _{0.5} Gd _{0.5} ScO ₃	Tb _{0.5} Dy _{0.5} ScO ₃
Space group	<i>Pnma</i> (No. 62)	<i>Pnma</i> (No. 62)
<i>a</i> /Å (powder)	5.73910(6)	5.72409(5)
<i>b</i> /Å (powder)	7.92445(10)	7.91013(8)
<i>c</i> /Å (powder)	5.47364(7)	5.45235(6)
<i>V</i> /nm ³	0.2489(1)	0.2468(1)
Formula units/cell	Z = 4	Z = 4
Crystal dimensions /μm ³	91 x 97 x 98	113 x 124 x 145
X-ray density /g•cm ⁻³	6.70(1)	6.83(1)
Reflection range	-14 < h < 14; -19 < k < 19; -13 < l < 13	-11 < h < 11; -15 < k < 15; -10 < l < 10
Refl. measured	75806	49706
Refl. unique	2126 (<i>R</i> _{int} = 0.043)	1088 (<i>R</i> _{int} = 0.057)
<i>wR</i> ₂	0.0288	0.0397
<i>R</i> _{obs} (<i>F</i> _o > 4σ(<i>F</i> _o))	0.0118	0.0167
<i>R</i> _{all}	0.0129	0.0182
Goodness of fit	1.272	1.373
Final ρ _{min} /10 ⁻³ e ⁻ nm ⁻³	-1.69	-1.42
Final ρ _{max} /10 ⁻³ e ⁻ nm ⁻³	3.11	3.42

107 Table 2: Room-temperature atomic and equivalent isotropic displacement parameters [Å²] of
 108 the given solid solutions obtained from single crystal X-ray diffraction data refinements.
 109

Atom	Wyckoff	<i>Pnma</i>	Occup	X	Y	z	U _{eq}
Tb _{0.5} Gd _{0.5} ScO ₃ : CSD-No 434171*							
Tb/Gd	4c	.m.	0.5/0.5	0.06010(2)	¼	0.48358(2)	0.0513(1)
Sc	4a	-1		0	0	0	0.0370(2)
O1	4c	.m.		0.44811(15)	¼	0.37863(16)	0.0604(9)
O2	8d	1		0.30539(11)	0.06352(9)	0.19148(11)	0.0734(7)
Tb _{0.5} Dy _{0.5} ScO ₃ : CSD-No 434170*							
Tb/Dy	4c	.m.	0.5/0.5	0.06090(2)	¼	0.48282(2)	0.0548(1)
Sc	4a	-1		0	0	0	0.0405(4)

O1	4c	.m.	0.44495(23)	$\frac{1}{4}$	0.37542(25)	0.0606(18)
O2	8d	1	0.30621(17)	0.06506(13)	0.19011(17)	0.0761(13)

*Further details, including anisotropic displacement parameters could be obtained from FIZ Karlsruhe, 76344 Eggenstein-Leopoldshafen, Germany (fax: (+49)7247-808-666; E-Mail: crysdata@fiz-karlsruhe.de, on quoting the deposition numbers CSD.

110 X-ray powder diffraction data were collected on a X'Pert MPD PRO diffractometer (PANalytical
 111 GmbH, Almelo, The Netherlands) equipped with Ni-filtered $\text{CuK}_{\alpha 1,2}$ radiation ($\lambda_{\text{K}\alpha 1} =$
 112 $1.5405929(5) \text{ \AA}$, $\lambda_{\text{K}\alpha 2} = 1.544414(2) \text{ \AA}$) and a X'Celerator detector system in $\theta/2\theta$ Bragg-Brentano
 113 geometry. Room-temperature scans were performed from 5 to 135° 2θ with a step width of
 114 0.0167° 2θ and a measurement time of 120 s per step. For the data collection the samples were
 115 finely ground firstly in a ball mill and secondly in an agate mortar under acetone. The obtained
 116 data were refined using the Rietveld method (DIFFRAC PLUS TOPAS V4.2, Bruker AXS, Karlsruhe,
 117 Germany). For profile fitting the fundamental parameter approach was used. The fundamental
 118 parameters for the in-house data were fitted against a LaB_6 standard material. As starting model
 119 the obtained single crystal parameters were used. The occupancy between Tb^{3+} and Gd^{3+} or Dy^{3+}
 120 on the 4c position were not refined.

121

122 2.3 Thermal analysis methods

123 Melting points were determined with a NETZSCH STA429C thermal analyzer. Crystalline pieces
 124 of 60 - 80 mg of pure rare-earth scandates and their solid solutions were placed in tungsten
 125 crucibles and covered by a tungsten lid to reduce heat exchange by thermal radiation.
 126 Temperature and DTA signal were measured with W/Re thermocouples and the vacuum-tight
 127 DTA furnace was after repeated evacuation (ca. 2×10^{-6} mbar)/flushing (ca. 0.5 bar) cycles filled
 128 with 1 bar of 6N (99.9999% purity) helium and subsequently closed. Two subsequent
 129 heating/cooling cycles with 15 K/min were performed for each sample, and onset as well as
 130 melting peak width were determined with the NETZSCH Proteus analysis software.

131 It is known that W/Re thermocouples tend to degenerate during long and repeated measuring
 132 cycles at very high temperatures. This is related to the higher fugacity of Re as compared to W,
 133 which alters thermocouple composition and hence also their temperature-emf relationship ⁶.
 134 The degeneration results in a systematically underestimated experimental temperature, and the
 135 degree of underestimation rises with the number of measurements that were already
 136 performed. Depending on measurement time and temperature, downward shifts up to 1 K per
 137 heating run are possible. To countervail this effect, a pure Al_2O_3 sample with true melting point
 138 $T_f = 2327 \text{ K}$ was measured from time to time. The difference between the experimental melting
 139 temperature and T_f was used for the correction of subsequent sample runs. Nevertheless, the
 140 instable temperature-emf relationship together with the higher noise/signal ratio at very high T
 141 $> 2300 \text{ K}$ results in less reliable data, compared to lower temperatures where Pt-based
 142 thermocouple can be used ⁷. Outgoing from this, the absolute temperature error of all melting

143 points given in this paper is estimated to ± 20 K. Inside one series the error is lower, and just
144 noisy DTA curves result in a scatter of maximum ± 5 K.

145 The specific heat capacity c_p as a function of the temperature T was measured by heat flux
146 differential scanning calorimetry (DSC) with a NETZSCH STA449C. For this purpose, three DSC
147 measurements were performed: first with an empty crucible as baseline correction, second with
148 Al_2O_3 powder as reference and third with the sample to analyze ⁸. The heat capacity was then
149 calculated by comparison of the obtained curves using the DIN 51007 method. Samples of the
150 solid solution crystals were pestled to crush and four subsequent heating runs (20 K/min) from
151 313 K to 1473 K were carried out in Pt crucibles with lids in flowing argon. Because the first run
152 showed higher experimental scatter and deviated by up to 15% from the following three runs,
153 solely the average values of the subsequent runs were used to determine $c_p(T)$.

154 Measurements of thermal diffusivity α were performed by laser flash technique with a NETZSCH
155 LFA427 on sample slices with thicknesses of approximately 1.5 mm and diameters between 6
156 and 12 mm, which were cut to give slice orientations (100), (010) or (001), respectively. For this
157 purpose, the samples were heated stepwise from 298 K to 1473 K, with a typical difference of
158 50 K between the steps. At every temperature step the bottom side of a sample was irradiated
159 three times by a Nd:YAG laser using a laser voltage of 460 V and a pulse width of 0.8 ms, which
160 results in a laser shot energy of approximately 4 J. The rise of the temperature on the top of the
161 sample was measured and the temperature time response was plotted to obtain $\alpha(T)$ from
162 Mehling's model ⁹ for semi-transparent media. To ensure uniform heat absorption, the samples
163 were covered with a thin layer of graphite prior to every measurement and a protective
164 atmosphere of flowing nitrogen was applied during the measurements to prevent oxidation of
165 that graphite layer. The thermal conductivity λ as a function of temperature T could then be
166 derived from the thermal diffusivity $\alpha(T)$, because these two properties are linked by
167

$$\lambda(T) = \rho(T) \cdot c_p(T) \cdot \alpha(T) \quad (1)$$

168 where c_p is the specific heat capacity and ρ the mass density ¹⁰. Table 3 lists the data used for ρ
169 and an average linear expansion coefficient $\bar{\alpha}$, which was used to model the temperature
170 dependence of the density and the samples thickness. These properties were calculated from
171 the data of related rare-earth scandates by using the average values between the endmembers
172 (TbScO_3 and DyScO_3 for $\text{Tb}_{0.5}\text{Dy}_{0.5}\text{ScO}_3$, TbScO_3 and GdScO_3 for $\text{Tb}_{0.5}\text{Gd}_{0.5}\text{ScO}_3$). These calculated
173 data that are given in Table 3 differ only by ca. 1.5% from the X-ray densities in Table 1.

174

175 Table 3: Mass density ρ and average linear expansion coefficient $\bar{\alpha}$ of the investigated solid
176 solutions, calculated from the data of related rare-earth scandates.

Crystal	ρ (g/cm ³) ^{11, 12}	$\bar{\alpha}$ (10 ⁻⁶ K ⁻¹) ^{3, 13}
$\text{Tb}_{0.5}\text{Dy}_{0.5}\text{ScO}_3$	6.725	8.3
$\text{Tb}_{0.5}\text{Gd}_{0.5}\text{ScO}_3$	6.605	9.6

177

178

179 3. Results and discussion

180

181 3.1 Grown crystals

182

183 $Tb_xGd_{1-x}ScO_3$ and $Tb_xDy_{1-x}ScO_3$ solid-solution single crystals with diameters of 18 mm and total
184 lengths of 53 - 55 mm were grown by using the Czochralski technique. $Tb_xDy_{1-x}ScO_3$ (Fig. 2a)
185 shows a yellow coloration, similar to $DyScO_3$. A slight brownish coloration was observed in the
186 central part of the crystal, which is most likely related to traces of Tb^{4+} . $Tb_xGd_{1-x}ScO_3$ (Fig. 2b)
187 shows a soft yellow-brown tone of homogenous appearance. The grown solid solutions were
188 found to be highly transparent for the major part of the boules. The lower part towards the tail
189 end of the crystal showed indication of scattering centers. The appearance of such scattering
190 centers is well known for several rare earth scandates and is typically attributed to the
191 incorporation of homogeneously nucleated nanocrystals of the same composition. This can be
192 potentially entirely suppressed by growing the crystals in a higher axial thermal gradient, as
193 shown by Uecker et al. for $GdScO_3$ ³.

194



195

196

197 Fig. 2 (a) $Tb_xDy_{1-x}ScO_3$ and (b) $Tb_xGd_{1-x}ScO_3$ solid-solution single crystals grown by the
198 Czochralski method.

199

200 3.2 Chemical composition and lattice parameters

201

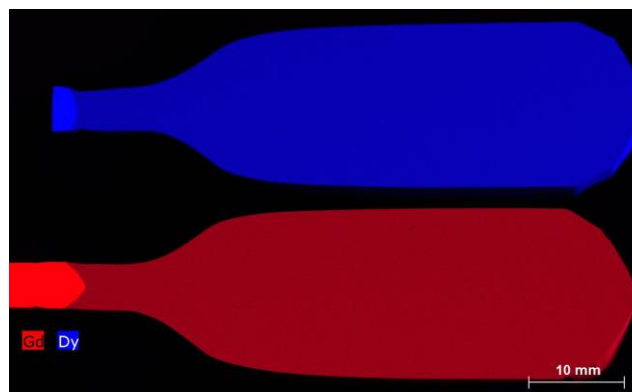
202 The chemical homogeneity of the crystals at the macroscopic and microscopic scale is relatively
203 high for this size of boules. This was confirmed by standard-calibrated μ -XRF mappings (Fig. 3)
204 and line scans (Fig. 4). In table 4, the chemical composition is summarized for seed-near parts
205 and for the tails. As can be seen, for the mixed crystals the maximum deviation differs only

206 about 0.25 at% between the first and last solidified parts of the crystals. When comparing the
 207 crystal compositions with initial melt compositions it is obvious, that the effective partition
 208 coefficients are larger than unity for Sc and lower than unity for Tb, Gd and Dy. This is
 209 explainable, since for the accessible members of the RE scandates the congruent melting
 210 composition is shifted from the stoichiometric composition to RE:Sc ratios slightly smaller than
 211 unity³. The results show that the composition shift along the growth axis is very low (Fig. 4), but
 212 it must be kept in mind if ultra-fine-tuning of lattice parameters is intended, and especially if
 213 much larger crystals are required. For simplicity reasons, the offsets from the nominal
 214 compositions are neglected in the following paragraphs.

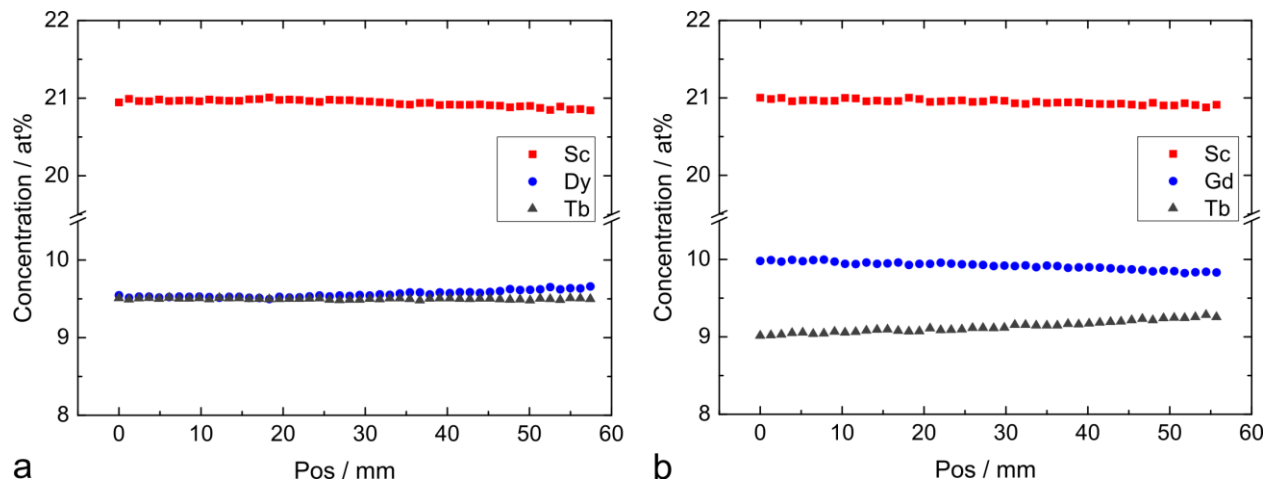
215
 216 Table 4: Chemical composition of the crystals measured by μ -XRF in comparison to the initial
 217 melt compositions.

Crystal	Tb (at%)	Dy (at%)	Gd (at%)	Sc (at%)
initial melt composition*	9.84	10.16	-	20
Tb _x Dy _{1-x} ScO ₃ seed-near	9.50	9.53	-	20.97
Tb _x Dy _{1-x} ScO ₃ tail	9.50	9.65	-	20.85
initial melt composition	10	-	10	20
Tb _x Gd _{1-x} ScO ₃ seed-near	9.02	-	9.99	20.99
Tb _x Gd _{1-x} ScO ₃ tail	9.27	-	9.84	20.89

218 *Estimated composition resulted by back-melting of a DyScO₃ seed
 219



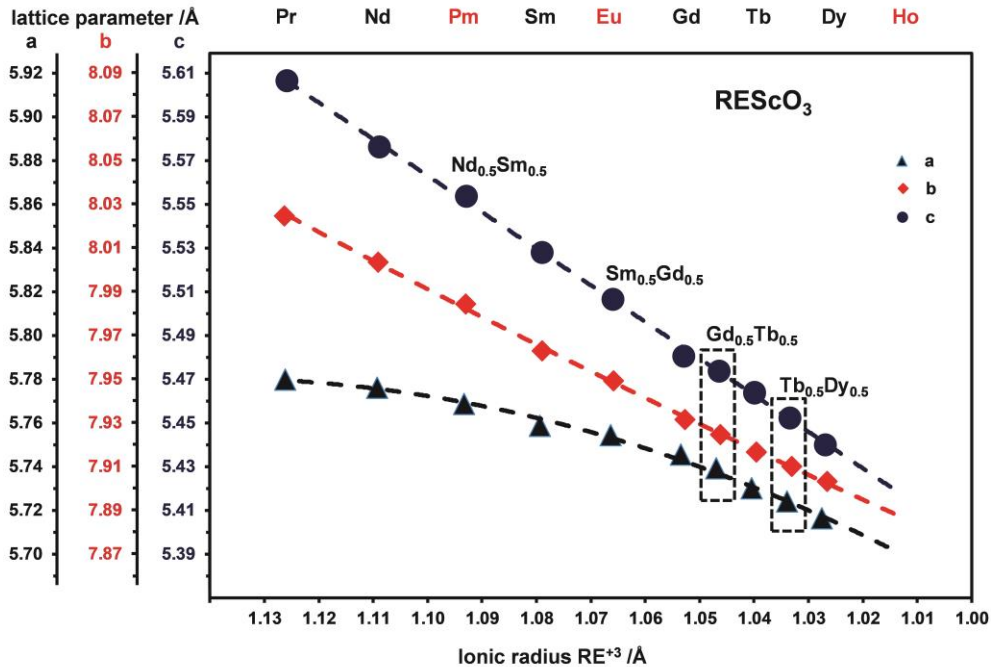
220
 221 Fig. 3 Gd-L α and Dy-L α X-ray fluorescence intensity map of the Tb_xDy_{1-x}ScO₃ and Tb_xGd_{1-x}ScO₃
 222 solid-solution single crystals.
 223



224 **a** **b**
 225 Fig. 4 Segregation profiles for $Tb_xDy_{1-x}ScO_3$ and $Tb_xGd_{1-x}ScO_3$ solid-solution single crystals.
 226

227 From the single crystal data it was not possible to refine the occupancy parameters of the rare
 228 earth metals on the $4c$ position in $Pnma$ independently. In all refinements the occupancy
 229 parameters for both lanthanides were set to 50% occupation each, close to the average crystal-
 230 chemical value. Small deviations do not affect the refinement results due to the negligible
 231 electron density difference resulting from the chemical composition. Accurate lattice
 232 parameters were determined from X-ray powder diffraction data Rietveld refinements. The
 233 obtained lattice parameters perfectly fit into the lattice parameter development of $REScO_3$ of
 234 the same crystal structure published by Uecker et al. ¹ as can be seen in Fig. 5.

235
 236
 237



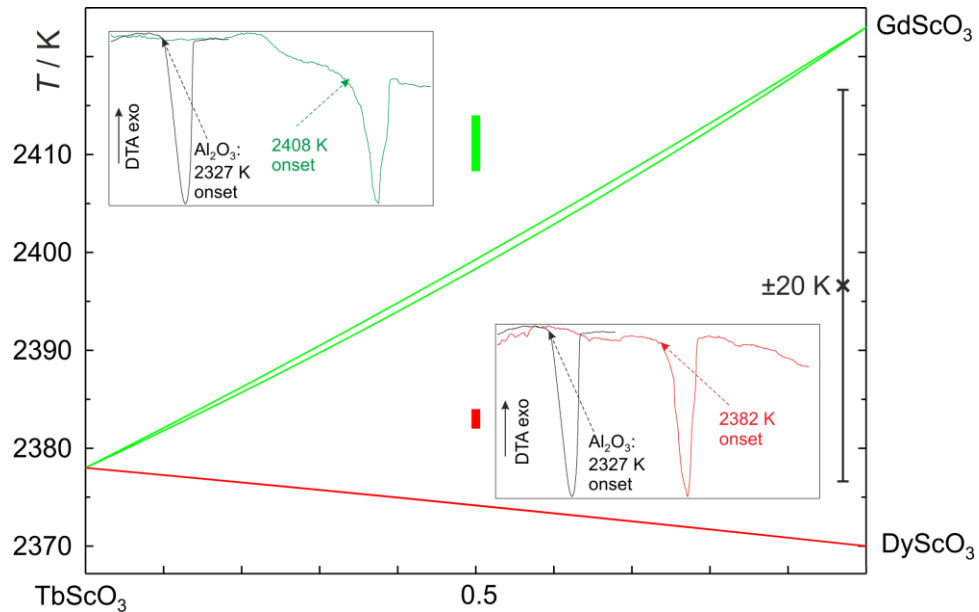
238
 239 Fig 5. Lattice parameter development of REScO₃ obtained by Uecker et al.¹ and in this study
 240 (dashed-line rectangles).
 241

242 3.3 Melting behavior

243
 244
 245 Badie¹⁴ reported for GdScO₃ and DyScO₃ melting points of (2423±20) K and (2373±20) K,
 246 respectively. No data are given there for TbScO₃. The melting point of GdScO₃ could be
 247 confirmed in the current as well as in a recent study¹; besides the heat of fusion was estimated
 248 to $\Delta H \approx 85.4$ kJ/mol from the area of the melting peak. In the current study it was found that
 249 DyScO₃ melts 47 K lower than GdScO₃, which results in $T_f = 2370$ K for this compound, and from
 250 the peak area $\Delta H \approx 89.3$ kJ/mol can be estimated. For TbScO₃ we reported previously 2368 K¹
 251 which is in fairly good agreement with current measurements resulting in $T_f = (2378 \pm 20)$ K and
 252 $\Delta H \approx 97.4$ kJ/mol for TbScO₃.

253 Assuming ideal behavior of the rare-earth scandate melts and solid solutions, theoretical
 254 TbScO₃-DyScO₃ or TbScO₃-GdScO₃ phase diagrams (Fig. 6) can be calculated with the Schröder-
 255 van-Laar equation^{1, 15}. Because the melting points of TbScO₃ (2378 K) and DyScO₃ (2370 K) are
 256 similar, liquidus and solidus are extremely flat and almost identical: at intermediate 2374 K
 257 solidus and liquidus are calculated at molar fractions of 0.519 and 0.523, respectively. Actually
 258 the melting point difference is smaller than the experimental error that amounts to ±20 K, as
 259 indicated close to the right temperature axis. The experimental melting peaks of a
 260 (Dy_{0.5}Tb_{0.5})ScO₃ mixed crystal starts just 8 K above the theoretical curve, which is still inside the
 261 limits of experimental accuracy. As to be expected, the melting peak is very narrow.

262 GdScO₃, in contrast, melts 45 K higher than TbScO₃ – resulting in a slightly broader
 263 liquidus/solidus span. Here the experimental melting range of the (Gd_{0.5}Tb_{0.5})ScO₃ mixed crystal
 264 starts ca. 6 K above the calculated curves. The insert shows that this mixed crystal has a slightly
 265 broader melting peak, which agrees with the calculated phase diagram and makes such crystals
 266 slightly more prone to Tb/Gd segregation.
 267



268
 269
 270 Fig. 6: Lines represent calculated phase diagrams TbScO₃-DyScO₃ or TbScO₃-GdScO₃,
 271 respectively. Experimental melting ranges of (Gd_{0.5}Tb_{0.5})ScO₃ and (Dy_{0.5}Tb_{0.5})ScO₃ mixed crystals
 272 are indicated as bars, together with DTA raw data in the inserts.
 273
 274
 275
 276
 277

278 3.4 Specific heat and thermal conductivity

279
 280

281 The DSC measurements revealed a smooth and monotonously rising behavior for the specific
 282 heat capacity $c_p(T)$ from room temperature to 1473 K. As expected, the DSC curves showed no
 283 spikes, indicating that no phase transition occurred over the investigated temperature range. A
 284 reasonably good fit of the experimental data for $c_p(T)$ could be obtained by usage of a
 285 polynomial function of type (2). Fit parameters a, b and c are given in Table 5.
 286

$$c_p(T) = a + b \cdot T + \frac{c}{T^2} \quad (2)$$

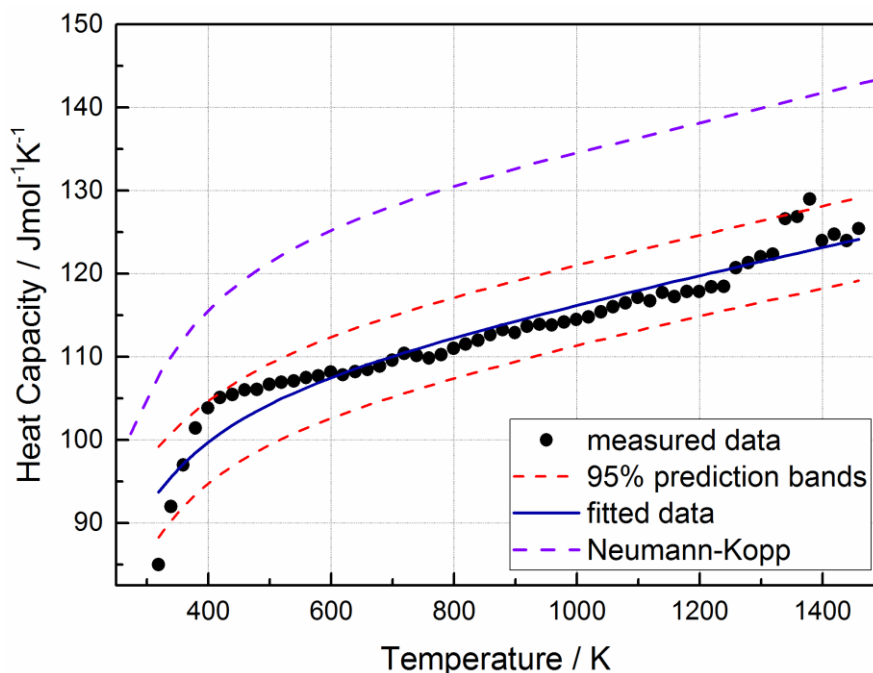
287 Table 5: Fit parameter a, b and c and coefficient of determination R² for the c_p(T) function (2) of
 288 the investigated rare-earth scandates.

289

Solid solution	Parameter			
	a	b	c	R ²
Tb _{0.5} Dy _{0.5} ScO ₃	101.645	1.5863 x 10 ⁻²	-1.32108 x 10 ⁶	0.9202
Tb _{0.5} Gd _{0.5} ScO ₃	111.714	5.7873 x 10 ⁻³	-2.31395 x 10 ⁶	0.9553

290

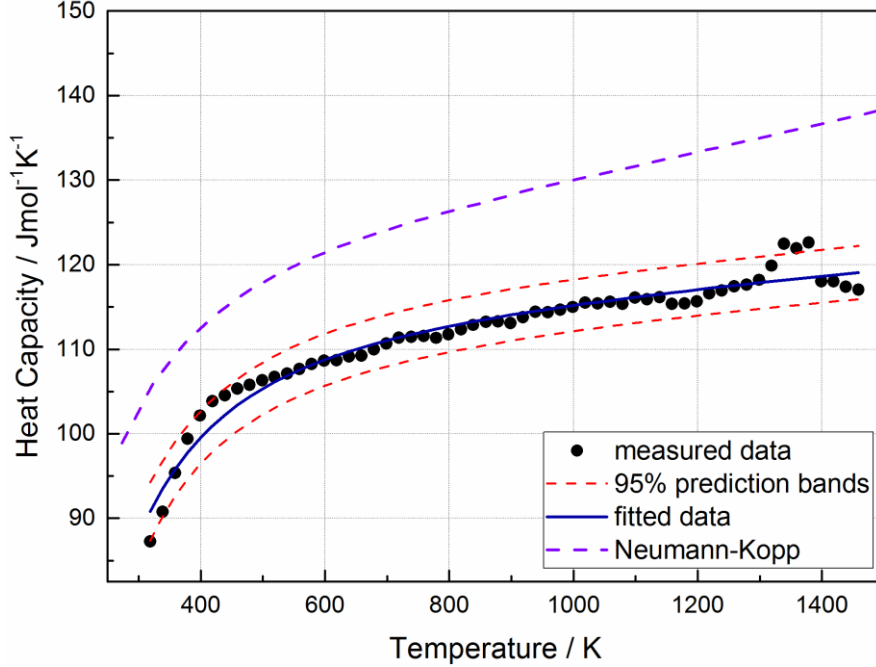
291 Often, a good theoretical approximation of c_p(T) can be obtained by application of the
 292 Neumann-Kopp rule, which estimates the heat capacity of complex oxides by using the
 293 weighted sum of heat capacities of their constituent binary oxides¹⁶. In this study, experimental
 294 data correlate satisfactorily with that theoretical estimation, showing only a slight deviation of
 295 about 10 - 15%. The lower experimental values are probably attributed to the reaction energy
 296 for the formation of each respective oxide, which is not considered by the Neumann-Kopp rule.
 297 Figures 7 and 8 show experimental data for c_p(T) that are fitted to equation (2). The theoretical
 298 approximation by application of the Neumann-Kopp rule is added for comparison.



299

300 Figure 7: Measured c_p(T) data of Tb_{0.5}Dy_{0.5}ScO₃ together with a fit to equation (2) and 95%
 301 prediction bands. For comparison c_p(T) data calculated according to the Neumann-Kopp rule are
 302 also shown.

303



304
 305 Figure 8: Measured $c_p(T)$ data of $Tb_{0.5}Gd_{0.5}ScO_3$ together with a fit to equation (2) and 95%
 306 prediction bands. For comparison $c_p(T)$ data calculated according to the Neumann-Kopp rule are
 307 also shown.
 308

309 Thermal conductivity $\lambda(T)$ of the samples was calculated from the measured thermal diffusivity
 310 $\alpha(T)$ according to equation (1) using the fit for the experimental data of $c_p(T)$ (see Table 5). The
 311 samples showed λ values in the range of 1.7-2.7 $WK^{-1}m^{-1}$, which is significantly lower than for
 312 most other functional oxides. Most remarkable is the unusual increase of $\lambda(T)$ at temperatures
 313 above 900 K. Recently, a similar behavior was observed for $TbScO_3$ and $DyScO_3$ crystals, but not
 314 for $GdScO_3$ ¹⁷. For many isolators thermal conductivity is dominated by phonon heat transport,
 315 which typically results in a decrease of λ at higher temperatures, because scattering reduces the
 316 phonon mean free path¹⁸. 1911 Eucken discovered an empirical law where thermal conductivity
 317 behaves inversely proportional to the temperature¹⁹. This $\lambda \propto 1/T$ law could be reproduced by
 318 theoretical consideration of three-phonon scattering events by Peierls 1929²⁰ and holds for
 319 many materials. However, if four-phonon processes are taken into account, higher exponents
 320 are needed to describe the temperature dependence of λ . Hofmeister et al. proposed a formula
 321 of the type (3) where a; b and c are constants²¹.
 322

$$\lambda(T) = \frac{1}{a+b \cdot T+c \cdot T^2} \quad (3)$$

323 Apparently, the $1/T$ law is insufficient to describe thermal conductivity of the studied
 324 compounds, because the increase of λ at elevated temperatures cannot be explained by that
 325 model. Recently, an analogous behavior of the thermal conductivity could be observed for the
 326 inverse spinel $MgGa_2O_4$ ²² as well as the pyrochlore $Tb_2Ti_2O_7$ ²³. For the spinel it was suggested,

327 that cations exchanging their site at elevated temperatures contribute to thermal transport.
 328 Thus, it seems plausible to consider transport of thermal energy in isolators through moving
 329 ions. An empirical formula with a linear term added to equation (3) can describe $\lambda(T)$ well (see
 330 equation (4)). Here the first inverse term describes the heat transport by phonons, while the
 331 second linear term might be related to transportation of thermal energy by any type of carriers
 332 ²³. At least for the RE₂ScO₇ a significant portion (ca. 4% for TbScO₃ ¹²) of the RE³⁺ sites is empty,
 333 which could enable diffusive movements of ions.

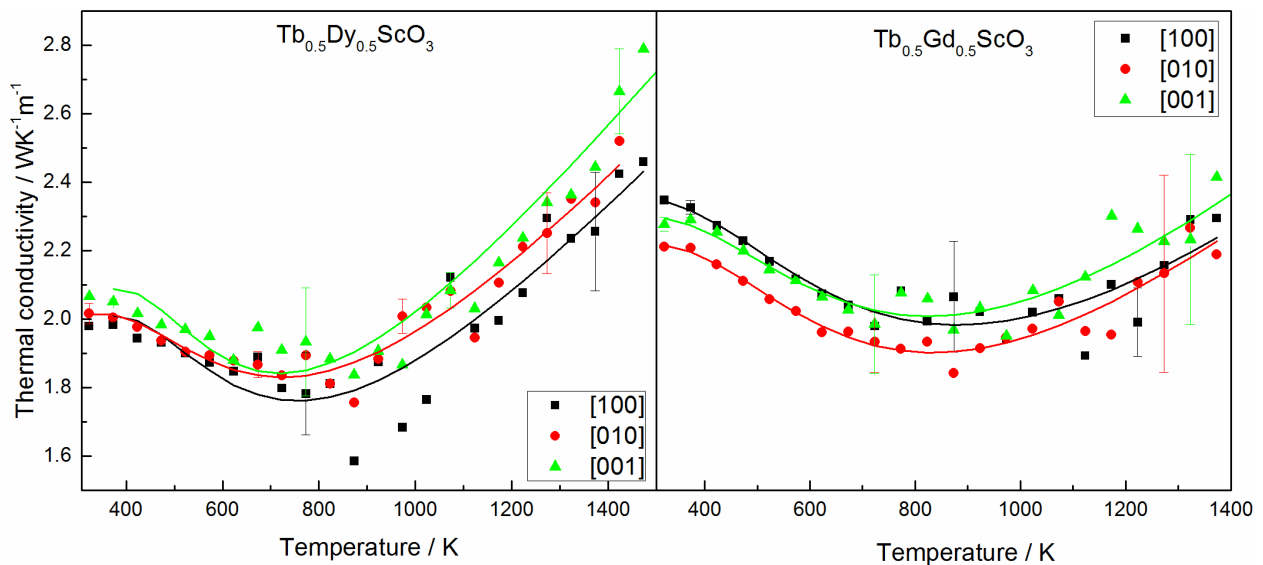
$$\lambda(T) = \frac{1}{a + b \cdot T + c \cdot T^2} + d \cdot T \quad (4)$$

334 In the current study, equation (4) was used to approximate the experimental data for the
 335 thermal conductivity. Fit Parameters for the investigated compounds are given in Table 6. In
 336 Figure 9 the experimental data for thermal conductivity are shown together with the
 337 corresponding fit functions.
 338

339 Table 6: Fit parameters and coefficient of determination R² for the $\lambda(T)$ function according to
 340 equation (4) of the investigated crystals.

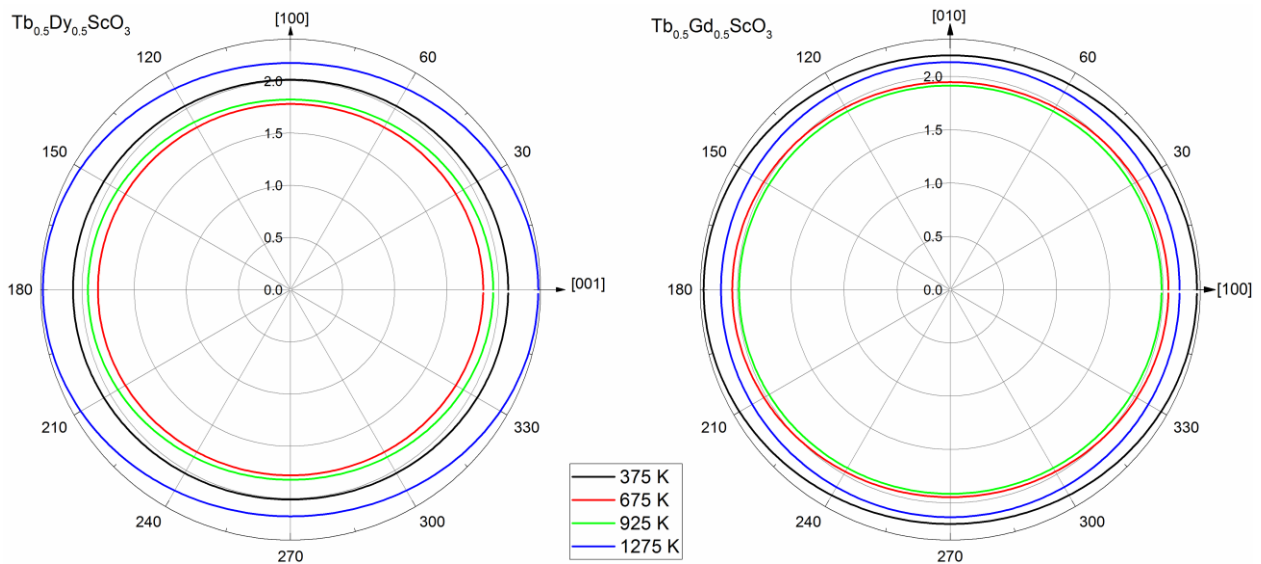
Compound	Parameter				
	a	b	c	d	R ²
Tb _{0.5} Dy _{0.5} ScO ₃ [100]	1.1393	-3.0745 × 10 ⁻⁰³	5.0871 × 10 ⁻⁰⁶	1.5617 × 10 ⁻⁰³	0.8482
Tb _{0.5} Dy _{0.5} ScO ₃ [010]	0.8759	-1.8419 × 10 ⁻⁰³	3.7127 × 10 ⁻⁰⁶	1.5994 × 10 ⁻⁰³	0.9288
Tb _{0.5} Dy _{0.5} ScO ₃ [001]	1.2818	-3.8956 × 10 ⁻⁰³	6.2305 × 10 ⁻⁰⁶	1.7448 × 10 ⁻⁰³	0.9431
Tb _{0.5} Gd _{0.5} ScO ₃ [100]	0.5396	-5.5818 × 10 ⁻⁰⁴	1.5934 × 10 ⁻⁰⁶	1.3669 × 10 ⁻⁰³	0.7903
Tb _{0.5} Gd _{0.5} ScO ₃ [010]	0.6308	-8.8290 × 10 ⁻⁰⁴	2.1344 × 10 ⁻⁰⁶	1.4110 × 10 ⁻⁰³	0.8926
Tb _{0.5} Gd _{0.5} ScO ₃ [001]	0.5679	-6.2699 × 10 ⁻⁰⁴	1.7547 × 10 ⁻⁰⁶	1.4607 × 10 ⁻⁰³	0.8081

341



342
 343 Figure 9: Thermal conductivity data of the two investigated rare-earth-scandates fitted with the
 344 function given by equation 4. The error bars indicate the doubled standard deviation.

345
 346 Like other transport properties, thermal conductivity is a symmetric second rank tensor and
 347 therefore consists of a maximum of six independent components. This number can even be
 348 reduced by consideration of the crystal symmetry²⁴. For orthorhombic crystals only the three
 349 diagonal components are independent, while off-diagonal elements are zero²⁵. Since the
 350 investigated rare-earth scandates are orthorhombic perovskites²⁶, this means that three
 351 components of thermal conductivity need to be measured in order to describe the
 352 corresponding conductivity tensor. Both mixed crystals revealed a relatively low anisotropy,
 353 exceeding not more than 15% as the biggest difference between the orientations. For
 354 $Tb_{0.5}Dy_{0.5}ScO_3$ the [001] direction was found to have the highest thermal conductivity followed
 355 by [010] as the medium, and [100] showing the lowest values for λ . $Tb_{0.5}Gd_{0.5}ScO_3$ reveals a
 356 different trend. At lower temperatures the sequence $\lambda^{[100]} > \lambda^{[001]} > \lambda^{[010]}$ was found, while for $T >$
 357 900 K $\lambda^{[001]}$ seems to become larger than $\lambda^{[100]}$. Figure 10 illustrates the anisotropy of these rare-
 358 earth scandates as a cross section through the representation surface of the thermal
 359 conductivity tensor perpendicular [010] for $Tb_{0.5}Dy_{0.5}ScO_3$ and [001] for $Tb_{0.5}Gd_{0.5}ScO_3$.



360
 361 Figure 10: Cross section through the representation surface of the thermal conductivity tensor
 362 of the investigated rare-earth scandates along the [001]-[100] plane for $Tb_{0.5}Dy_{0.5}ScO_3$ and the
 363 [100]-[010] plane for $Tb_{0.5}Gd_{0.5}ScO_3$. Radial units are $WK^{-1}m^{-1}$.

364 365 366 367 4. Conclusion and outlook

368
 369 The Czochralski method is suitable for growing $Tb_xGd_{1-x}ScO_3$ and $Tb_xDy_{1-x}ScO_3$ solid-solution
 370 single crystals with diameters of 18 mm and cylindrical lengths of about 40 mm. Investigations
 371 of segregation revealed a minor composition shift along the growth axis, which is expected to

372 be minimized by growing the next-generation crystals from melts with RE:Sc ratios slightly
373 smaller than unity, where congruent melting occurs for the RE scandate endmembers.

374 Based on previous developments for DyScO₃, TbScO₃ and GdScO₃ it seems possible that both
375 solid solutions can be potentially upscaled to larger sizes exceeding one inch in diameter.

376 The calculated TbScO₃-DyScO₃ and TbScO₃-GdScO₃ phase diagrams can be used to estimate the
377 maximum expected segregation of solid-solution crystals for slightly scandium oxide enriched
378 melts (for starting materials containing about 21 at% Sc) and based on Vegard's rule to predict
379 the required starting composition for any desired pseudo-cubic lattice parameter in the range of
380 3.9486 and 3.9678 Å. Within the accessible members of the REScO₃ family (RE = Dy to Pr) only
381 Pr_xNd_{1-x}ScO₃ mixed crystals are still missing, but due to small differences in RE ionic radii,
382 isomorphous crystal structures and congruent melting endmembers no major difficulties are
383 expected.

384

385 Acknowledgements

386

387 The authors are grateful to R. Bertram for performing ICP-OES measurements and to I. M.
388 Schulze-Jonack, E. Thiede, M. Rabe, M. Imming-Friedland, V. Lange and T. Wurche for technical
389 assistance and material preparation.

390

- 391 1. R. Uecker, D. Klimm, R. Bertram, M. Bernhagen, I. Schulze-Jonack, M. Brützam, A. Kwasniewski,
392 T. M. Gesing and D. G. Schlom, *Acta Physica Polonica A*, 2013, 124, 295-300.
- 393 2. K. J. Hubbard and D. G. Schlom, *Journal of Materials Research*, 2011, 11, 2757-2776.
- 394 3. R. Uecker, B. Veličkov, D. Klimm, R. Bertram, M. Bernhagen, M. Rabe, M. Albrecht, R. Fornari and
395 D. G. Schlom, *J. Crystal Growth*, 2008, 310, 2649-2658.
- 396 4. R. Uecker, H. Wilke, D. G. Schlom, B. Velickov, P. Reiche, A. Polity, M. Bernhagen and M.
397 Rossberg, *J. Crystal Growth*, 2006, 295, 84-91.
- 398 5. G. Sheldrick, *Acta Crystallographica Section A*, 2008, 64, 112-122.
- 399 6. G. W. Burns and M. G. Scroger, *National Institute of Standards and Technology*, 1989, 25-25.
- 400 7. D. Klimm, R. Bertram, Z. Galazka, S. Ganschow, D. Schulz and R. Uecker, *Cryst. Res. Technol.*,
401 2012, 47, 247-252.
- 402 8. M. J. O'Neill, *Analytical Chemistry*, 1966, 38, 1331-1336.
- 403 9. H. Mehling, G. Hautzinger, O. Nilsson, J. Fricke, R. Hofmann and O. Hahn, *Intern. J.*
404 *Thermophysics*, 1998, 19, 941-949.
- 405 10. W. J. Parker, R. J. Jenkins, C. P. Butler and G. L. Abbott, *J. Appl. Phys.*, 1961, 32, 1679-1684.
- 406 11. B. Veličkov, V. Kahlenberg, R. Bertram and M. Bernhagen, *Z. Krist.*, 2007, 222, 466-473.
- 407 12. B. Veličkov, V. Kahlenberg, R. Bertram and R. Uecker, *Acta Cryst. E*, 2008, 64, i79-i79.
- 408 13. M. D. Biegalski, J. H. Haeni, S. Trolier-McKinstry, D. G. Schlom, C. D. Brandle and A. J. V. Graitis,
409 *Journal of Materials Research*, 2005, 20, 952-958.
- 410 14. J. M. Badie, *Rev. int. Hautes Temp. Réfract., Fr.*, 1978, 15, 183-199.
- 411 15. J. J. v. Laar, *Z. Phys. Chem.*, 1908, 63, 216-253.
- 412 16. E. van Aubel, *Ann. Phys.*, 1901, 309, 420-421.
- 413 17. J. Hidde, C. Gugushev, S. Ganschow and D. Klimm, *J. Alloys. Compd.*, 2018, 738, 415-421.
- 414 18. G. A. Slack, *Phys. Rev.*, 1962, 126, 427-441.
- 415 19. A. Eucken, *Ann. Phys.*, 1911, 339, 185-221.

- 416 20. R. Peierls, *Ann. Phys.*, 1929, 395, 1055-1101.
- 417 21. A. M. Hofmeister, *Phys. Chem. Min.*, 2006, 33, 45-62.
- 418 22. L. Schwarz, Z. Galazka, T. M. Gesing and D. Klimm, *Cryst. Res. Technol.*, 2015, 50, 961-966.
- 419 23. D. Klimm, C. Guguschev, D. J. Kok, M. Naumann, L. Ackermann, D. Rytz, M. Peltz, K. Dupre, M. D.
420 Neumann, A. Kwasniewski, D. G. Schlom and M. Bickermann, *CrystEngComm*, 2017, 19, 3908-
421 3914.
- 422 24. R. E. Newnham, *Properties of Materials: Anisotropy, Symmetry, Structure*, Oxford University
423 Press, 2005.
- 424 25. H.-R. Wenk and A. Bulakh, *Minerals: Their Constitution and Origin*, Cambridge University Press,
425 2012.
- 426 26. R. P. Liferovich and R. H. Mitchell, *J. Solid State Chem.*, 2004, 177, 2188-2197.
- 427